Composite Structures

An experimental and numerical study on scaling effects in the low velocity impact response of CFRP laminates

Z. Xu [a], F. Yang [a], Z.W. Guan [a,*], W.J. Cantwell [b]

[a] School of Engineering, University of Liverpool, Liverpool L69 3GH, UK
[b] Department of Aerospace Engineering, Khalifa University, Abu Dhabi, United Arab Emirates

ABSTRACT

Scaling effects in the low velocity impact response of plain weave carbon-fibre-reinforced plastic (CFRP) panels have been investigated both experimentally and numerically. The experimental tests were undertaken using an instrumented drop-weight impact tower and the numerical simulations were conducted using the commercially-available finite element (FE) solver ABAQUS/Explicit. Here a rate-dependent damage model was implemented through the ABAQUS user-defined material interface, VUMAT, to describe the mechanical behaviour of the composite laminates. The experimental tests and numerical simulations both indicate that at energies above the damage threshold, damage does not obey a simple scaling law, becoming more severe as the scale size is increased. An examination of the damaged samples in the tests and numerical simulations indicated that, for a given scaled impact energy, fibre damage, in the form of large cracks extending in the warp and weft directions, was more severe in the larger samples. It is argued that the energy absorbed in fibre fracture scales with the square of the scale factor, i.e. n^2, whereas the initial impact energy scales as n^3. This discrepancy results in increased levels of energy needing to be absorbed in larger scale sizes, leading to greater levels of impact damage in the larger scale sizes.

1. Introduction

Obtaining a clear understanding of size effects in the mechanical response of structures is a necessary prerequisite for the successful design of load-bearing engineering components. Early attempts focused on a range of relatively simple metal structures. Jones [1] studied scaling effects in the impact response of steel structures and demonstrated that, under particular conditions, traditional scaling laws are not satisfied due to the strain-rate sensitivity of steel. Duffey et al. [2] developed a series of dimensionless groups based on the Buckingham-Π theorem to study scaling effects in a number of dynamically-loaded structures.

As a result of the rapid expansion of the use of composite materials in aerospace design, a number of detailed studies have been conducted to investigate size effects in the strength of fibre reinforced composites [3–5]. Kellas et al. [3,4] employed the Buckingham-Π theorem to study scaling effects in carbon/epoxy composites, observing significant size effects in the strength of their samples. Wisnom [5] identified a size dependency in the

bending strength of a unidirectional carbon fibre/epoxy system. Several workers have also investigated scaling effects in the impact behaviour of composite materials [6–10]. Morton applied the Buckingham-Π theorem to study size effects in the impact response of a number of carbon-fibre composite laminates with different stacking sequences [6]. Here, it was shown that the impact force scaled as the scale factor squared, while the impact duration scaled as the scale factor. It was observed that the strength of the composite laminates decreased significantly with an increase in specimen size. Swanson [8] conducted a significant number of impact tests (approximately 600), to study scaling effects in the impact response of CFRP. The study involved tests on small laboratory specimens (CFRP plates) to large structures (CFRP cylinders) based on the Ritz procedure and the Fourier series expansion respectively. It was found that the delamination size exhibited a dependence on scaling size, whereas the values of fibre failure stress and strain were independent of specimen size.

The aim of this work is to employ both experimental and numerical techniques to investigate scaling effects in plain weave CFRP composite panels subjected to low-velocity impact. Particular attention is paid to the investigation of size-related effects in the impact load-displacement responses and the resulting impact damage within the composite panels.

---

* Corresponding author.
  E-mail address: zguan@liv.ac.uk (Z.W. Guan).

2. Similitude study

The similitude approach adopted in this work describes a geometrical scaling law for predicting the response parameters based on a set of well-defined input parameters. The former, known as output parameters, generally include the deflection of the target or structure, the impact load, the contact time between the impactor and target, and the stress-strain or load-deflection response within the model. The latter, also known as input parameters, typically include a characteristic length, L, that effectively defines the scaling size of each scale model. The material input parameters are related to the mechanical properties, as well as the density of the material. The dimensions of these input and output parameters along with the relations of these parameters with respect to the scale factor n (defined as the ratio of the characteristic length in the scale model to that in the full-scale model) are given in Table 1. When conducting scaled impact tests of this nature, it is worth noting that the mass of the drop-weight carriage should scale as the cube of the scale factor, whereas the impact velocity should keep constant for all tests.

3. Experimental procedure

The CFRP plates used in the current tests were fabricated from EP121-C20-53 prepregs supplied by Gurit Ltd. The EP121-C20-53 prepreg consists of a 3k HTA carbon-fibre plain weave fabric pre-impregnated within a 45% EP121 epoxy resin. The plain weave fabric has an areal density of 204 g/m^2 and the epoxy resin is a highly toughened system with curing temperatures between 120 °C and 160 °C. In its as-supplied form, the prepreg has a nominal thickness of 0.25 mm.

Tests were undertaken on scaled CFRP panels, these being ¼, ½, ¾, and full-scale samples manufactured from 4, 8, 12, and 16 layers of EP121-C20-53 plies respectively. The dimensions of the CFRP panels are given in Table 2, where it should be noted that the edge dimensions of the plates were 65, 130, 195 and 260 mm for the four scale sizes.
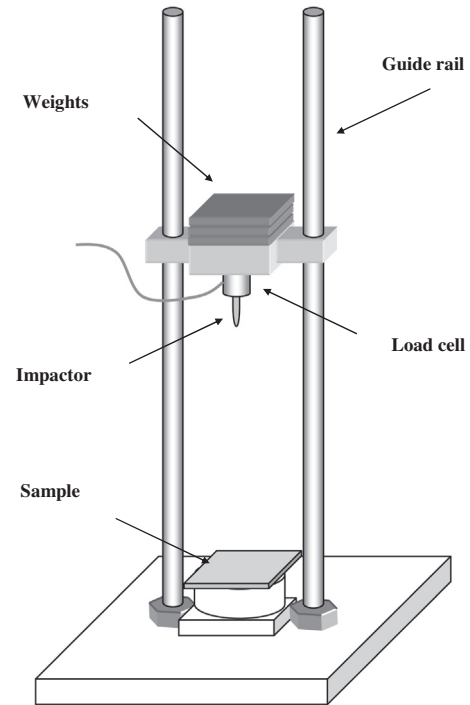
The low velocity impact response of the scaled composite plates was investigated using the drop-weight impact tower shown in Fig. 1. The scaled panels were simply supported (without clamping) using four scaled steel rings with inner diameters of 50, 100, 150 and 200 mm. Four scaled hemispherical indentors, with diameters of 5, 10, 15 and 20 mm, were employed to test the four scaled specimens. The release height for all tests was 500 mm, giving an impact velocity of approximately 3.13 m/s for all tests. The force-time history was recorded using a Kistler 9021A piezo-electric load cell, with a 35 kN capacity, located just above the indentor. The velocity and displacement of the indentor and the sample deformation were captured using a high speed camera, positioned in front of the drop-weight impact tower. High speed footage was recorded at 10,000 frames per second and the resulting images were analysed using the motion analysis software ProAnalyst.

Table 1
Summary of the impact test parameters and their dependency on the scale factor n.

Parameter	Scaling Factor
Panel thickness	n
Diameter of indentor	n
Support ring size	n
Edge length	n
Impact mass	n^3
Impact energy	n^3
Impact contact duration	n
Maximum impact force	n^2
Target displacement	n
Damage area	n^2

Table 2
Dimensions of the scaled CFRP plates as well as the impact testing conditions.

Scale factor n	Edge length (mm)	Avg. thickness (mm)	No. of plies	Drop height (mm)	Indentor diameter (mm)	Internal diameter of support ring (mm)
1/4	65	1.12	4	500	5	50
1/2	130	2.24	8	500	10	100
3/4	195	3.36	12	500	15	150
1	260	4.48	16	500	20	200

Fig. 1. Schematic of drop-weight impact tower.

4. Finite element modelling

A number of FE models were created using the ABAQUS modelling package to supplement the experimental investigation. The dimensions of these models were the same as those of the samples in the experimental tests. Each of these FE models consisted of an indentor, a deformable CFRP panel and a support (shown in Fig. 2a), where both the indentor and the support were modelled using rigid surfaces and the CFRP panel was modelled as a homogeneous, orthotropic material, the behaviour of which will be discussed in the next section.

To save computational cost, the falling motion of the indentor was replaced by positioning the indentor to be just in contact with the top surface of the CFRP panel, whilst applying both an initial velocity v_I, equal to 3.13 m/s, and a scaled point-mass m_n, to the reference point of the indentor. The scaled point-mass of the impactor was approximated by:

$$m_n = 2E_n/v_I^2$$

where E_n is the scaled energy.

In addition, the CFRP panel was discretised using 8-noded linear brick (C3D8) elements with a very dense mesh design (shown in Fig. 2b) for regions that potentially involved contact and damage. This was done to ensure a reasonable degree of accuracy in the resulting predictions. A graded-coarse mesh was used for the
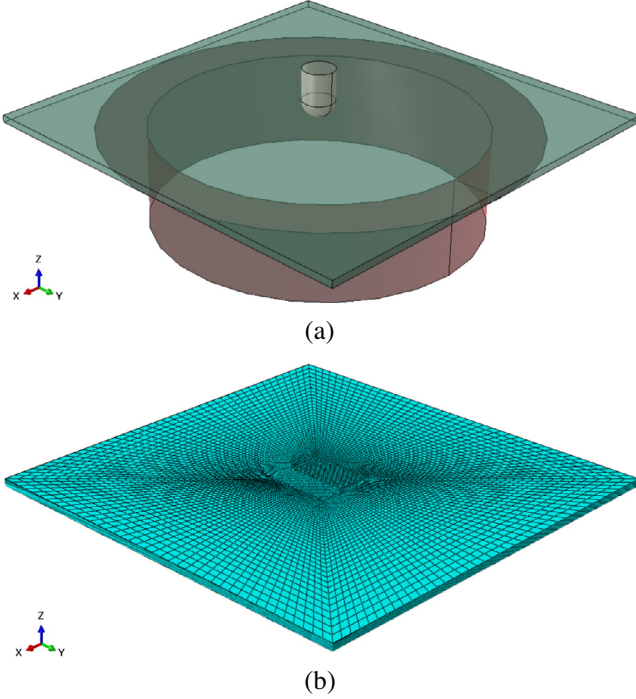
Fig. 2. (a) Geometry of the FE model, (b) mesh design for the CFRP panel.

remaining areas, to reduce computational time. Further, in the potential contact domain, a set of elements, that includes not only the exterior elements, but also the interior elements, was created for defining a surface-to-element interaction between the indentor and the element set, such that the contact of the indentor with the interior elements after complete failure of the exterior elements can also be guaranteed.

4.1. Material modelling

4.1.1. Elastic behaviour

The composite panels used in the experiment were fabricated from plain weave fabric prepregs, featuring similar mechanical response in the warp and weft direction. Thus, it is assumed herein that the CFRP material is a homogeneous, transversely isotropic material, with an elastic response prior to damage initiation and thereafter an anisotropic damage evolution. By using 1, 2 and 3 to denote the in-plane warp, in-plane weft and out-of-plane directions of the plain weave CFRP material, the elastic constitutive relation between stress and strain can be expressed as:

$$\boldsymbol{\sigma} = \mathbf{C}_0 \boldsymbol{\varepsilon} \tag{1}$$

where

$$\boldsymbol{\sigma} = \{ \sigma_{11} \quad \sigma_{22} \quad \sigma_{33} \quad \tau_{12} \quad \tau_{23} \quad \tau_{31} \}^T \tag{2}$$

$$\boldsymbol{\varepsilon} = \{ \varepsilon_{11} \quad \varepsilon_{22} \quad \varepsilon_{33} \quad \varepsilon_{12} \quad \varepsilon_{23} \quad \varepsilon_{31} \}^T \tag{3}$$

$$\mathbf{C}_0 = \mathbf{S}_0^{-1} = \begin{bmatrix} \frac{1}{E_1} & -\frac{v_{21}}{E_2} & -\frac{v_{31}}{E_3} & 0 & 0 & 0 \\ -\frac{v_{12}}{E_1} & \frac{1}{E_2} & -\frac{v_{32}}{E_3} & 0 & 0 & 0 \\ -\frac{v_{13}}{E_1} & -\frac{v_{23}}{E_2} & \frac{1}{E_3} & 0 & 0 & 0 \\ 0 & 0 & 0 & \frac{1}{G_{12}} & 0 & 0 \\ 0 & 0 & 0 & 0 & \frac{1}{G_{23}} & 0 \\ 0 & 0 & 0 & 0 & 0 & \frac{1}{G_{31}} \end{bmatrix}^{-1} \tag{4}$$

where $\mathbf{C}_0$ is the elastic, or stiffness matrix, $\mathbf{S}_0$ is the compliance matrix, E_i refers to the Young's modulus in direction i, v_{ij} is the Poisson's ratio corresponding to the contraction in direction j caused by the tension in direction i, and G_{ij} is the shear modulus in the $i-j$ plane.

4.1.2. Failure criteria

The failure of plain weave composites subjected to low-velocity impact can be characterised using the well-established criteria proposed by the Materials Science Corporation [11] and the University of Delaware [12]. These criteria are essentially a generalised form of Hashin's failure criteria [13] for unidirectional composites; that is, a set of quadratic failure functions is employed to determine damage initiation related to all potential failure modes. In this work, the above failure criteria were adopted with some minor modifications and are briefly presented as follows.

Fibre tensile/shear failures in the warp (f_{1T}) and weft (f_{2T}) directions are defined based on the quadratic interaction between the corresponding axial stress and the shear stresses:

$$f_{1T} = \left\{ \frac{\sigma_{11}}{S_{1T}} \right\}^2 + \left\{ \frac{\tau_{12}}{S_{12}} \right\}^2 + \left\{ \frac{\tau_{31}}{S_{31}} \right\}^2 - 1 = 0, \quad \sigma_{11} > 0 \tag{5}$$

$$f_{2T} = \left\{ \frac{\sigma_{22}}{S_{2T}} \right\}^2 + \left\{ \frac{\tau_{12}}{S_{12}} \right\}^2 + \left\{ \frac{\tau_{23}}{S_{23}} \right\}^2 - 1 = 0, \quad \sigma_{22} > 0 \tag{6}$$

where S_{1T} and S_{2T} are the tensile strengths in the associated directions, and S_{12}, S_{23} and S_{31} are the layer shear strengths corresponding to the shear failure in the warp and weft directions.

In-plane compressive fibre failure (e.g. fibre buckling or kinking) in the warp (f_{1C}) and weft (f_{2C}) directions is jointly determined by the associated axial stress and the out-of-plane normal stress:

$$f_{1C} = \left(\frac{-\sigma_{11} + \langle -\sigma_{33} \rangle}{S_{1C}} \right)^2 - 1 = 0, \quad \sigma_{11} < 0 \tag{7}$$

$$f_{2C} = \left(\frac{-\sigma_{22} + \langle -\sigma_{33} \rangle}{S_{2C}} \right)^2 - 1 = 0, \quad \sigma_{22} < 0 \tag{8}$$

where S_{1C} and S_{2C} are the tensile strengths in the associated directions, and denote Macaulay brackets.

Crush failure (f_{3C}) related to out-of-plane impact is given by:

$$f_{3C} = \left(\frac{\langle p \rangle}{S_{3C}} \right)^2 - 1 = 0, \quad p = -\frac{\sigma_{11} + \sigma_{22} + \sigma_{33}}{3} < 0 \tag{9}$$

where S_{3C} is the crush strength.

In the absence of fibre breakage, the in-plane shear stress can cause matrix failure within the woven fabric:

$$f_{12} = \left(\frac{\tau_{12}}{S_{12}} \right)^2 - 1 = 0 \tag{10}$$

The matrix material can also fail in the through-the-thickness direction due to the through-the-thickness stresses, and its failure can be defined using:

$$f_{3T} = \left\{ \frac{\sigma_{33}}{S_{3T}} \right\}^2 + \left\{ \frac{\tau_{23}}{S_{23}} \right\}^2 + \left\{ \frac{\tau_{31}}{S_{31}} \right\}^2 - 1 = 0 \tag{11}$$

where S_{3T} is the through-the-thickness tensile strength. It is noted that such failure mode is also referred to delamination since the failure adjacent to the ply interface is likely to form a failure plane parallel to the layering planes. However, this failure mode is not considered in this work since the delamination of the composite material (EP121-C20-53, which is based on a heavily toughened epoxy resin) subjected to low-velocity impact is small, as shown in the optical micrograph in Fig. 3.

Fig. 3. Optical micrograph showing the damaged section of the n = 3/4 panel following test at a scaled energy of E = 97.22n³ Joules.

When subjected to impact, fibre-reinforced polymer composites generally exhibit rate-dependent mechanical properties, e.g. the strengths and elastic moduli increase with increasing strain-rate. Among different classes of fibre-reinforced composites, glass-fibre and aramid-fibre composites typically show relatively strong increases in their mechanical properties at higher strain rates; whereas the mechanical properties of carbon-fibre composites are generally strain-rate insensitive [14–16]. Based on this, the strain-rate effects on the mechanical properties of carbon-fibre composites can be neglected for the sake of simplicity.

4.1.3. Damage development

After damage initiation, the effective or damaged stiffness matrix $\mathbf{C}_d$ is modified to characterise the degradation of the material stiffness, and the constitutive relation between the stress $\boldsymbol{\sigma}$ and the strain $\boldsymbol{\varepsilon}$ is then given as:

$$\boldsymbol{\sigma} = \mathbf{C}_d \boldsymbol{\varepsilon} \tag{12}$$

where the damaged stiffness matrix $\mathbf{C}_d$ is defined as the inverse of the damaged compliance matrix $\mathbf{S}_d$:

$$\mathbf{C}_d = \mathbf{S}_d^{-1} = \begin{bmatrix} \frac{1}{(1-d_1)E_1} & -\frac{v_{21}}{(1-d_2)E_2} & -\frac{v_{31}}{(1-d_{3C})E_3} & 0 & 0 & 0 \\ -\frac{v_{12}}{(1-d_1)E_1} & \frac{1}{(1-d_2)E_2} & -\frac{v_{32}}{(1-d_{3C})E_3} & 0 & 0 & 0 \\ -\frac{v_{12}}{(1-d_1)E_1} & -\frac{v_{23}}{(1-d_2)E_2} & \frac{1}{(1-d_{3C})E_3} & 0 & 0 & 0 \\ 0 & 0 & 0 & \frac{1}{(1-d_{12})G_{12}} & 0 & 0 \\ 0 & 0 & 0 & 0 & \frac{1}{(1-d_2)G_{23}} & 0 \\ 0 & 0 & 0 & 0 & 0 & \frac{1}{(1-d_1)G_{31}} \end{bmatrix}^{-1} \tag{13}$$

where the cumulative damage values in the warp and weft directions are defined as:

$$d_1 = 1 - (1 - d_{1T})(1 - d_{1C}) \tag{14}$$

$$d_2 = 1 - (1 - d_{2T})(1 - d_{2C}) \tag{15}$$

The damage associated with the different failure modes can be updated in the following general form:

$$d_{ab}(t_n + \Delta t) = d_{ab}(t_n) + \Delta t \dot{d}_{ab} \tag{16}$$

where ab denotes the six failure modes, i.e. 1T, 1C, 2T, 2C, 3C and 12. In this work, the damage evolutions corresponding to these failure modes are defined as:

$$\dot{d}_{1T} = \frac{a_1}{\Delta t}\left[\left(\frac{\sigma_{11}}{S_{1T}}\right)^2 - 1\right] \quad \text{if } f_{1T} > 0, \ \Delta\varepsilon_{11} > 0 \tag{17}$$

$$\dot{d}_{1C} = \frac{a_1}{\Delta t}\left[\left(\frac{\sigma_{11}}{S_{1C}}\right)^2 - 1\right] \quad \text{if } f_{1C} > 0, \ \Delta\varepsilon_{11} < 0 \tag{18}$$

$$\dot{d}_{2T} = \frac{a_1}{\Delta t}\left[\left(\frac{\sigma_{22}}{S_{2T}}\right)^2 - 1\right] \quad \text{if } f_{2T} > 0, \ \Delta\varepsilon_{22} > 0 \tag{19}$$

$$\dot{d}_{2C} = \frac{a_1}{\Delta t}\left[\left(\frac{\sigma_{22}}{S_{2C}}\right)^2 - 1\right] \quad \text{if } f_{2C} > 0, \ \Delta\varepsilon_{22} < 0 \tag{20}$$

$$\dot{d}_{3C} = \frac{a_2}{\Delta t}\left[\left(\frac{\sigma_{33}}{S_{3C}}\right)^2 - 1\right] \quad \text{if } f_{3C} > 0, \ \Delta\varepsilon_{33} < 0 \tag{21}$$

$$\dot{d}_{12} = \frac{a_2}{\Delta t}\left[\left(\frac{\tau_{12}}{S_{12}}\right)^2 - 1\right] \quad \text{if } f_{12} > 0 \tag{22}$$

where a_1 and a_2 are two non-physical material parameters controlling the rates of damage evolution.

4.2. FE implementation

A VUMAT subroutine, that incorporates the above material model, was developed for the impact simulations. A flow chart for the VUMAT subroutine is shown in Fig. 4. As can be seen from the figure, each time ABAQUS/Explicit calls the subroutine, it passes information to the subroutine, including the material properties (E_i, G_{ij}, v_{ij} and $\mathbf{S} = \{S_{1T} \ S_{1C} \ S_{2T} \ S_{2C} \ S_{3C} \ S_{12} \ S_{23} \ S_{31}\}^T$), the strain increment of the current increment step $\Delta\varepsilon(t_{n+1})$, the time increment size Δt, and the state variables of the previous increment step, namely, strain $\varepsilon(t_n)$, and damage $d_{ab}(t_n)$. The material properties of the CFRP material are given in Table 3. Based on the inputted information, failure at any given material point can be determined using the failure criteria presented in Section 4.1.2, and the level of damage, if any, can be calculated using Eqs. (14)–(22). Subsequently, the constitutive stiffness matrix can be obtained using Eq. (4) or Eq. (12). Based on this, the stress associated with the current increment step, $\sigma(t_{n+1})$, can be updated and introduced into ABAQUS/Explicit. It is noted that the above procedure should loop over all of the integration points and all of the time increments.
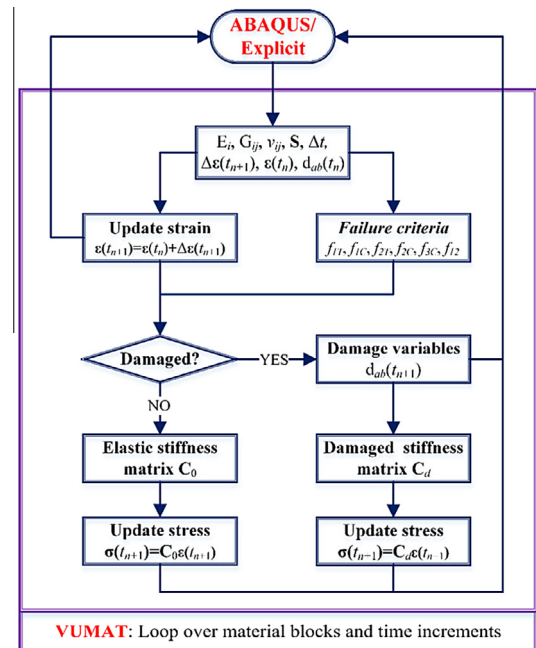
Fig. 4. Flow chart for the VUMAT subroutine.

**Table 3**
Material properties of the CFRP.

E_1 (GPa)	55	S_{1T} (MPa)	850
E_2 (GPa)	55	S_{1C} (MPa)	500
E_3 (GPa)	17	S_{2T} (MPa)	850
v_{12}	0.07	S_{2C} (MPa)	500
v_{23}	0.15	S_{3C} (MPa)	500
v_{31}	0.15	S_{12} (MPa)	120
G_{12} (GPa)	11.4	S_{23} (MPa)	65
G_{23} (GPa)	8.1	S_{31} (MPa)	65
G_{31} (GPa)	8.1	ρ (g/cm^3)	1.6

5. Results and discussion

Fig. 5a shows the experimental and predicted load-displacement traces for the plain composite plates following impact tests at an energy of $97.22n^3$ Joules. All four traces measured in the experimental tests exhibit similar responses, with the load increasing to a maximum, before tending to plateau around an approximately constant force. A subsequent examination of the samples highlighted the presence of fibre fracture extending in the warp and weft directions from the centre of the panel. It is believed that the maximum force observed in the load-displacement traces coincides with the initiation of lower surface fibre fracture, and the subsequent plateau value of force (highlighted by the arrowed line) is associated with this fibre damage extending away from the centre of the panel.

The load-displacement traces predicted by the FE simulations are similar to those observed following the tests, except for a small triangular-shaped peak prior to the plateau value, as observed experimentally. It is believed that this discrepancy is associated with the fact that delamination between composite plies (which was generally very limited as shown in Fig. 3) was not considered when modelling the CFRP, leading to an over-estimation of the stiffness of the panel, and consequently a higher reaction force during this phase of the impact event. By analysing the predicted stress and deformation response of the composite panel shown in Fig. 6, it is established that the maximum force in the
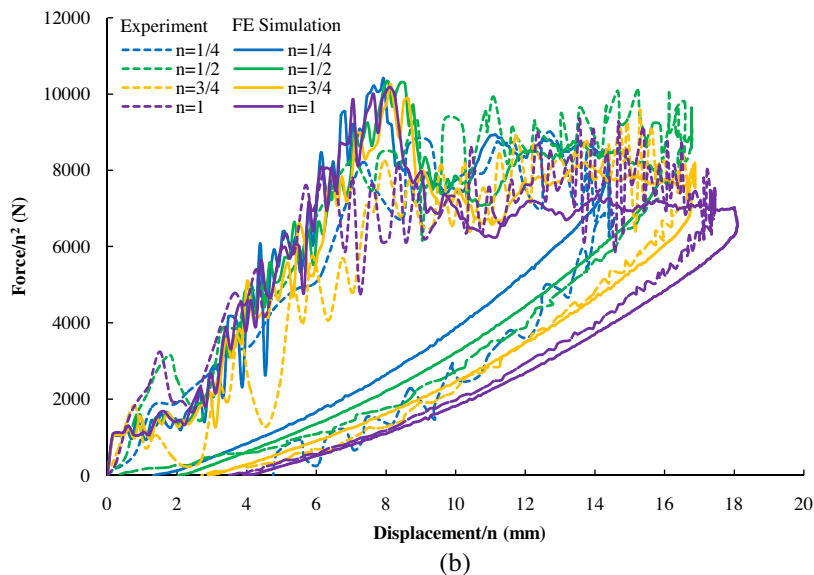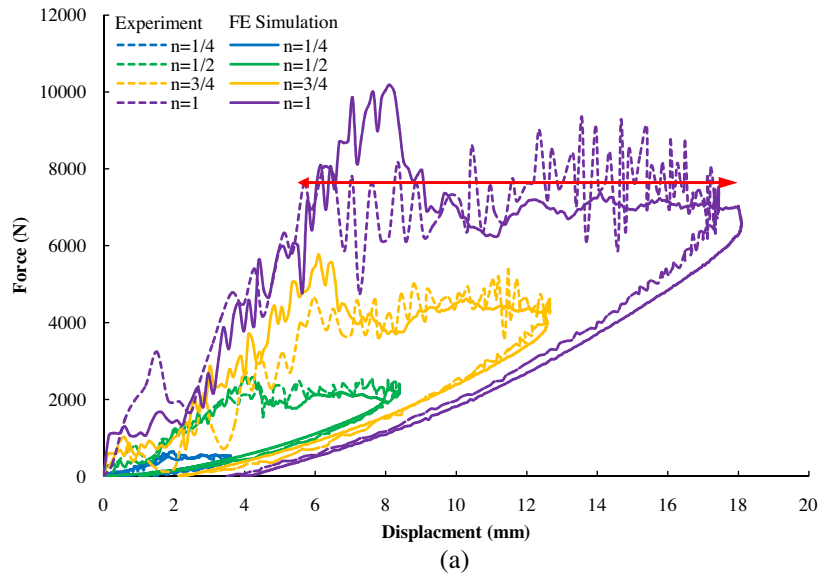
Fig. 5. (a) Load-displacement traces at a scaled energy of $E = 97.22n^3$ Joules (the arrow indicates the fibre fracture phase). (b) Corresponding normalised load-displacement traces.
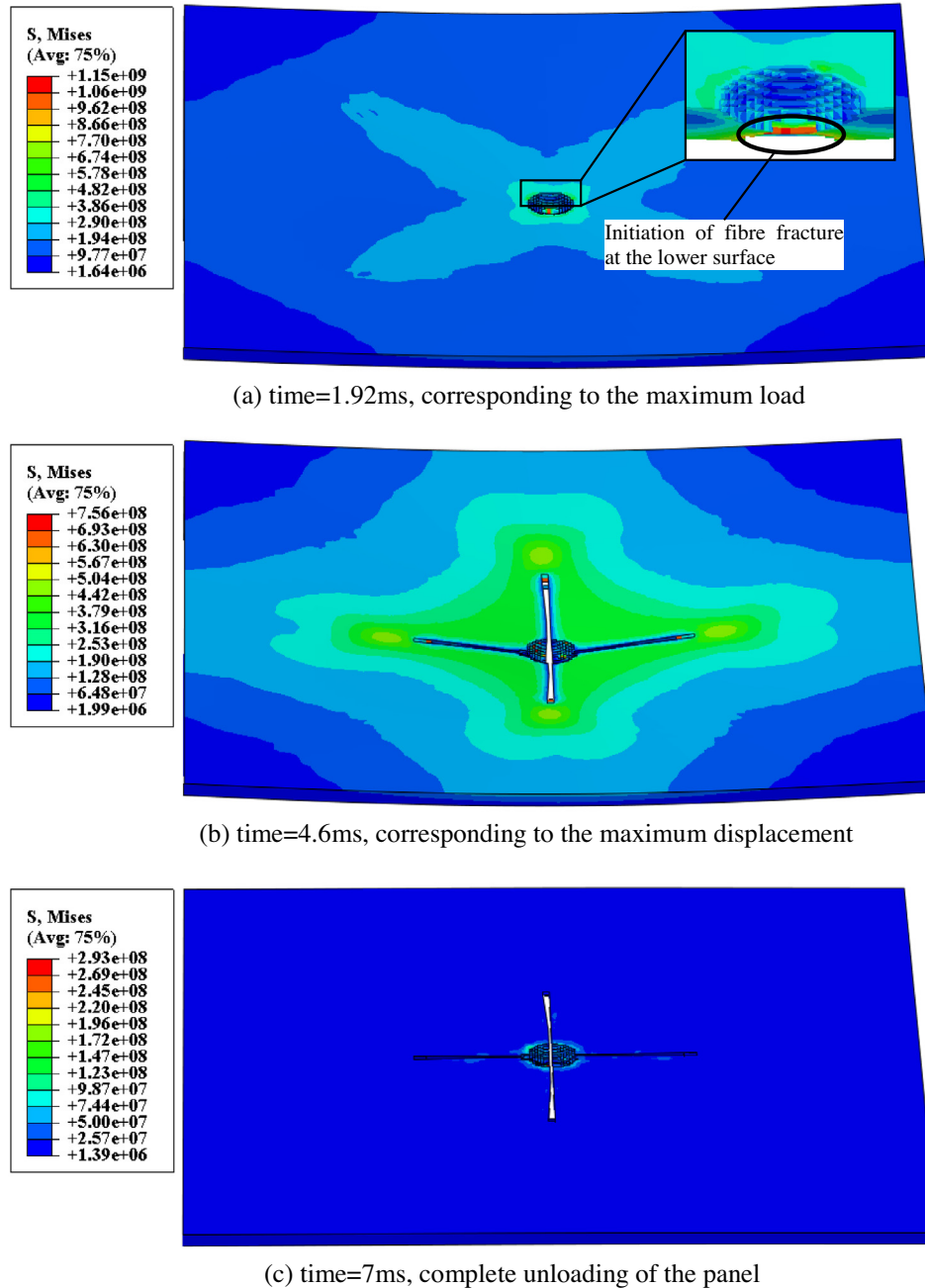
(a) time=1.92ms, corresponding to the maximum load

(b) time=4.6ms, corresponding to the maximum displacement

(c) time=7ms, complete unloading of the panel

Fig. 6. Stress and deformation profiles during different stages of the impact event for the $n = 1/2$ CFRP panel subjected to an impact energy of $E = 97.22n^3$.

load-displacement trace coincides with the initiation of the lower surface fibre fracture (see Fig. 6a) and that fibre fracture thereafter extends progressively in the warp and weft directions away from the centre of the panel, until the impactor reaches its maximum displacement (see Fig. 6b). By comparing Fig. 6b with Fig. 6c, it is evident that damage does not develop during the unloading phase. In order to investigate scaling effects, the load-displacement traces were normalised by dividing the force by the square of the scale size and the displacement by the scale size. Initial observations indicate that the resulting traces, Fig. 5b, exhibit a reasonable level of agreement, suggesting that simple scaling laws apply for this type of loading. However, closer scrutiny indicates that the fibre fracture phase tends to increase with scale size. This will be discussed in more detail below.

Fig. 7 shows the experimental and numerical load-displacement traces, as well as the normalised load-displacement plots, following impact tests at an energy equal to 128.4n³ Joules. Again the FE simulations are in reasonable agreement with the experimental traces, expect for the discrepancies around the maximum force value and the lower values of maximum displacement. The traces obtained using the two methods exhibit similar features, with the force increasing to a maximum point (associated with the fibre fracture threshold) followed by a region in which the force is highly oscillatory, associated with the propagation of fibre cracks in the warp and weft directions, away from the centre of the panel. The normalised data, Fig. 7b, indicate that the initial elastic portions of all traces appear to coincide, as does the peak force at the onset of fibre fracture. However, the deformation phase,
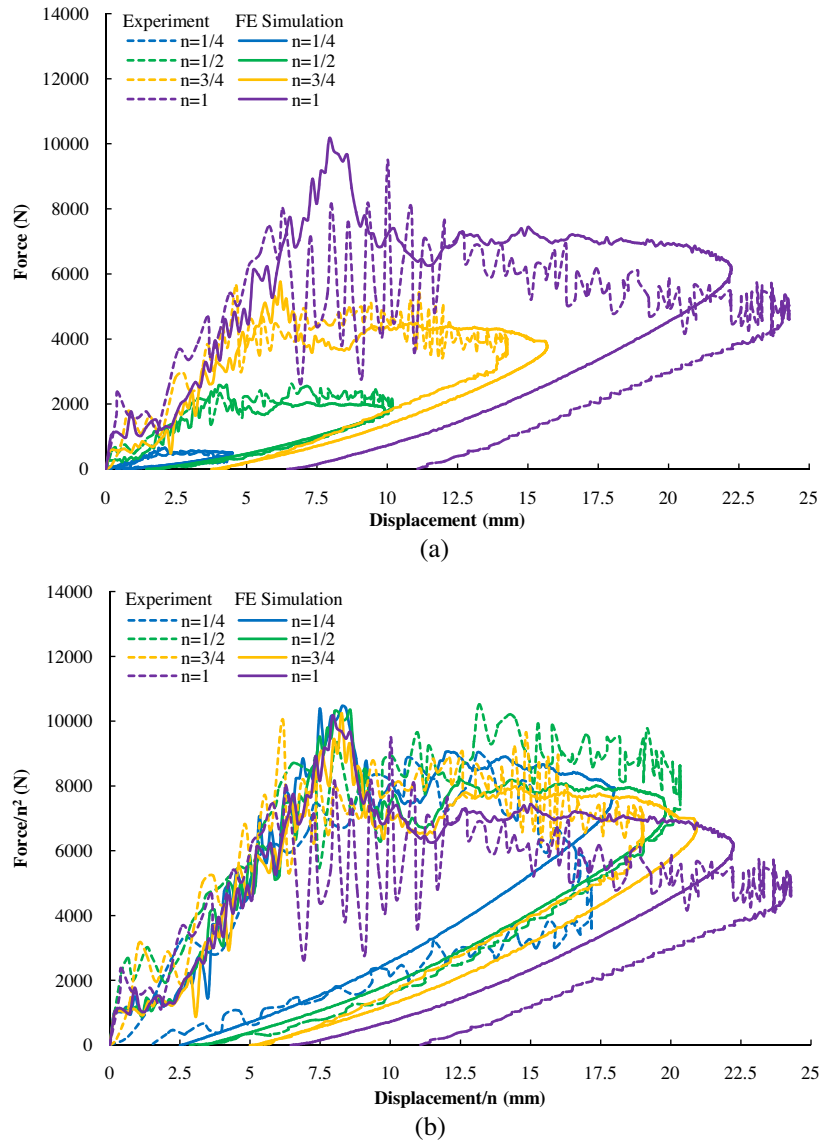
Fig. 7. (a) Load-displacement traces at a scaled energy of $E = 128.4n^3$ Joules. (b) Corresponding normalised load-displacement traces.
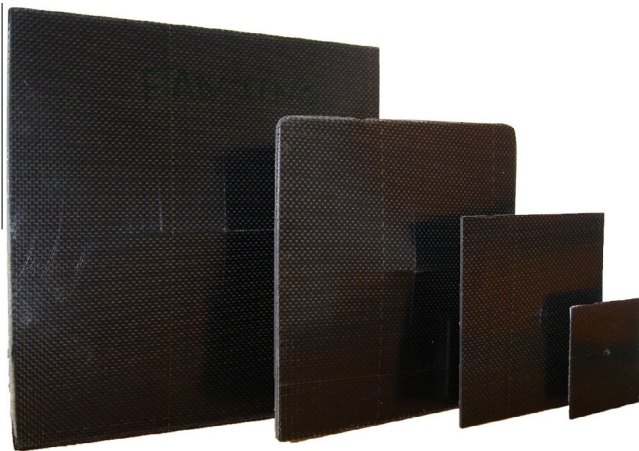

Fig. 8. Photographs of damaged panels following tests at a scaled impact energy of $E = 128.4n^3$ Joules.

associated with the aforementioned fibre fracture regime, again appears to increase with increasing panel size, resulting in an increase in measured maximum displacement in the larger panels.

Fig. 8 shows the rear surfaces of the four sizes of panel following an impact energy of $128.4n^3$ Joules. Closer examination of the panels highlights the presence of lines of fibre fracture in both the warp and weft directions. The severity (length, not width) of this rear surface fibre damage increased with panel size, with the relative crack lengths in the two directions increasing with scale size. This supports the conclusions made following observation of the load-displacement traces, where the length of the fibre fracture region was seen to increase with panel size. Only small levels of delamination were observed in these panels, due to the highly toughened nature of the epoxy matrix.

Fig. 9 shows both sets of normalised load-displacement traces following impact tests at an energy of $148.8n^3$ Joules. As before, the elastic response of the panels scales reasonably well, with all of the traces appearing to collapse onto a single curve. Beyond this initial elastic region, the traces again become highly oscillatory as the fibres within the laminate fracture. Closer examination of this damage phase again suggests that fibre damage is greater in larger
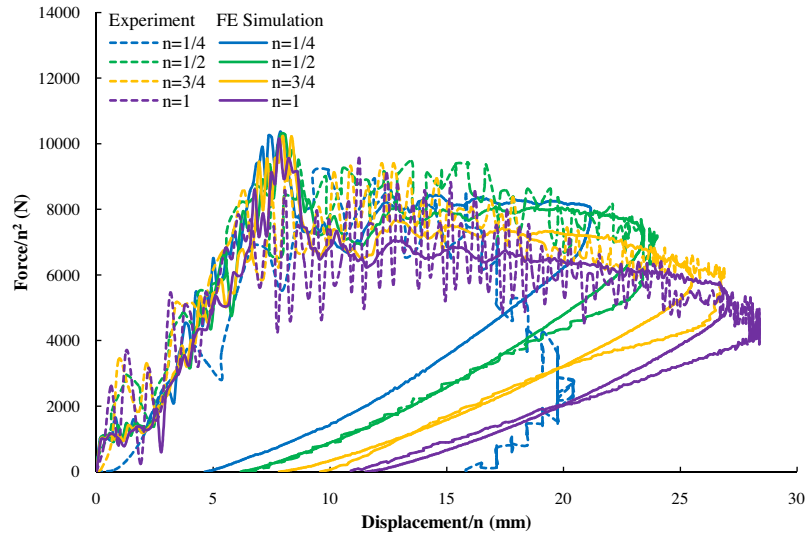
Fig. 9. Normalized load-displacement traces at a scaled energy of E = 148.8n^3 Joules.

samples. This effect was investigated in greater detail by measuring the effective impactor displacement associated with this form of failure in each of the normalised load-displacement traces, e.g. see the arrow in Fig. 5a. The resulting data is presented in Fig. 10. Here, it is clear that the size of this fibre fracture phase exhibits a strong dependency on scale size, with the length of this zone increasing rapidly with scale size. For example, for the highest impact energy (148.8n^3 Joules), this (scaled) region increases (from approximately 11 mm to 22 mm for the experimental tests and 13 mm to 19 mm for the FE simulations) in passing from the smallest to the largest scale sizes, suggesting that fibre damage should be more severe in larger samples.

The severity of damage in the laminates was characterised by measuring the total length of fibre fracture in both the warp and weft directions on the rear surface. This value was then normalised by dividing by twice the panel width. Fig. 11 shows the variation of these normalised crack length values with scale size for the four impact energies considered here, from where it is evident that damage does not obey a scaling law, with damage becoming more severe as the scale size is increased. Indeed, for a given impact energy, the normalised damage in the full-scale samples was

between two and three times that in the ¼ samples. It is interesting to note that the experimental trends are reproduced by the FE model, with damage becoming more severe with increasing scale size. These observations agree with the measurements from the normalised load-displacement plots shown previously, where the crack propagation phase was found to increase with scale size. The energy associated with fibre fracture will clearly depend on both the area of fibre fracture that is created, as well the fracture energy associated with this mode of failure. It should be noted that the physical width of the warp and weft fibre cracks were similar at all scale sizes, since the cracks propagated between individual tows. In simple terms, the energy associated with fibre fracture can therefore be estimated from:

$$E_f = tl\gamma \tag{23}$$

where γ is a fracture energy associated with failure in this fibre-dominated mode, t is the plate thickness and l is the length of fibre fracture. This term therefore scales with the square of scale size, i.e. n^2. It is clear that once the elastic energy absorbing capability of the target has been exceeded (a parameter that scales as n^3), additional energy must be absorbed in failure mechanisms, primarily fibre
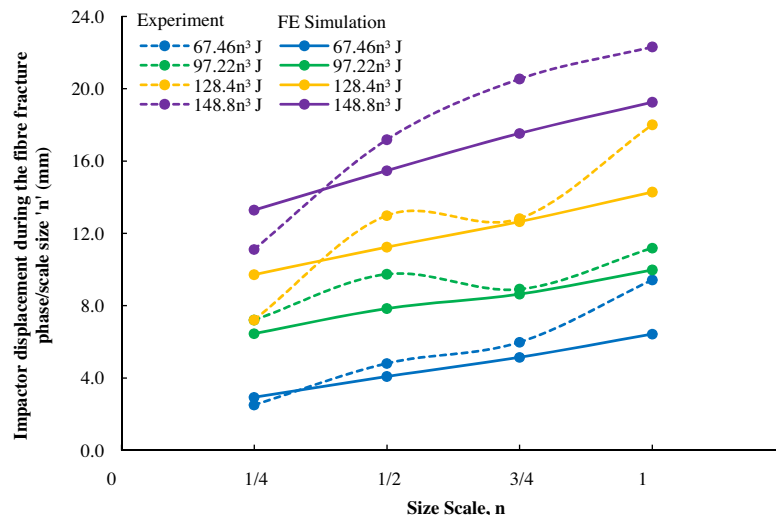

Fig. 10. The variation of the impactor displacement during the fibre fracture phase with scale size for the four scaled energies shown in the caption.
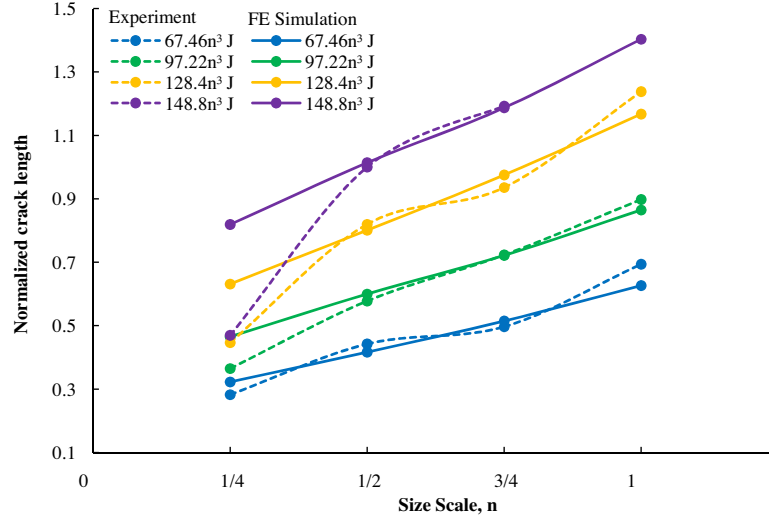
Fig. 11. The variation of the normalised crack length with scale size.
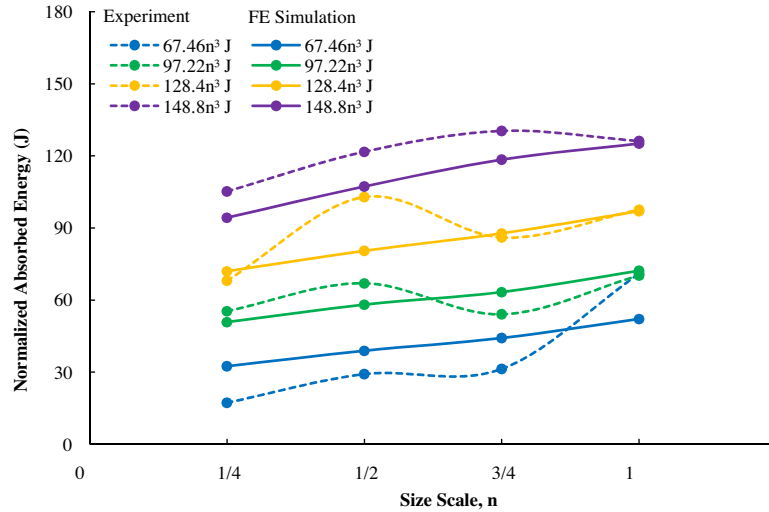

Fig. 12. The absorbed energy by the composite plates for different normalised impact energies.

fracture since the delamination resistance is high, as observed in all of the current panels. Given that the energy absorbed in the fibre failure process scales with n^2, whereas the incident energy scales as n^3, it is argued that larger zones of fibre fracture will be needed to absorb the 'additional' energy associated with impact on the larger panels. It is also worth pointing out that whereas membrane effect should be the same for all four sizes of panel when loaded elastically, they may play an increasing role is the larger panels following the onset of damage. Clearly, the normalised load-displacement traces indicate that the maximum panel displacement increases with scale size for a given scaled energy, suggesting that membrane stretching may further increase damage within the panels.

The evidence presented above clearly demonstrates that impact damage in these composites does not follow a simple scaling law, but becomes more severe with increasing scale size. The energy absorbed during the impact event was determined from the area under the load-displacement traces and these values are plotted as a function of scale size in Fig. 12. Although there is some scatter in the values of the absorbed energy measured in the experimental tests, particularly at the intermediate energies, the data associated with both the experimental tests and FE simulations do suggest that the absorbed energy increases with scale size for a given scaled impact energy. An examination of the figure indicates that the panels absorb almost all of the available incident energy at the highest energy levels. For example, at an energy of $148.8n^3$ Joules, the 1/4 scale sample absorbs approximately $108n^3$ Joules and the full scale panel absorbs approximately $130n^3$ Joules.

6. Conclusions

Scaling effects in the low velocity impact response of a carbon fibre reinforced plastic plates have been investigated through impact tests and finite element simulations. Agreement between the experimental tests and the predictions is reasonably good in most cases. Relatively small differences between the two sets of load-displacement traces are associated with the fact that delamination was not accounted for in the numerical model. The impact tests on the composite plates have shown that the elastic response of the panels obeys a scaling law. In contrast, damage does not scale according to that predicted by simple scaling laws. An examination of the damaged panels has shown that, for a given scaled

impact energy, fibre fracture is more severe in larger panels. These observations were again supported by the predictions from the finite element models. It is argued that beyond the threshold for damage initiation, the energy absorbed in fibre fracture scales with the square of the scale size, n^2, whereas as the energy introduced into the target increases according to n^3. This additional energy is absorbed by creating longer fibre cracks that extend away from the central point of impact.

Acknowledgement

References

[1] Jones N. Scaling of inelastic structures loaded dynamically. In: Davies GAO, editor. Structural impact and crashworthiness, vol. 1. London and New York: Elsevier Appl. Sci.; 1984. p. 45–74.

[2] Duffey TA, Cheresh MC, Sutherland SH. Experimental verification of scaling laws for punch-impact-loaded structures. Int J Impact Eng 1984;2(1):103–17.

[3] Kellas S, Morton J. Strength scaling in fiber composites. NASA CR 4335; 1990.

[4] Jackson KE, Kellas S, Morton J. Scale effects in the response and failure of fiber reinforced composite laminates loaded in tension and in flexure. J Comput Mater 1992;26(18):2674–705.

[5] Wisnom MR. The effect of specimen size on the bending strength of unidirectional carbon fibre-epoxy. Comput Struct 1991;18(1):47–63.

[6] Morton J. Scaling of impact-loaded carbon-fiber composites. AIAA J 1988;26 (8):989.

[7] Qian Y, Swanson SR, Nuismer RJ, Bucinell RB. An experimental study of scaling rules for impact damage in fiber composites. J Comput Mater 1990;24 (5):559–70.

[8] Swanson SR. Scaling of impact damage in fiber composites from laboratory specimens to structures. Comput Struct 1993;25(1–4):249–55.

[9] Pintado P, Morton J. On the scaling of impact loaded composite beams. Comput Struct 1994;27(4):357–65.

[10] Dorey G. Impact and crashworthiness of composite structures. In: Davies GAO, editor. Structural impact and crashworthiness. Elsevier Applied Science; 1984.

[11] LS-DYNA Keyword User's Manual, Livermore Software Technology Corporation, Version 971; 2007.

[12] University of Delaware, MAT162 Software, Available at <http://www.ccm.udel.edu/software/mat162> [Accessed:18 May 2016].

[13] Hashin Z. Failure criteria for unidirectional fiber composites. J Appl Mech 1980;47:329–34.

[14] Rotem A, Lifshitz JM. Longitudinal strength of unidirectional fibrous composite under high rate of loading. In: Proceedings of the 26th annual technical conference, society for plastic industry, reinforced plastics/composites division, Washington DC, Section 10-G. p. 1–10.

[15] Armenakas AE, Sciammarella CA. Response of glass-fiber-reinforced epoxy specimens to high rates of tensile loading. Exp Mech 1973;13:433–40.

[16] Chamis CC, Smith GT. Environmental and high strain rate effects on composites for engine applications. AIAA J 1984;22:128–34.